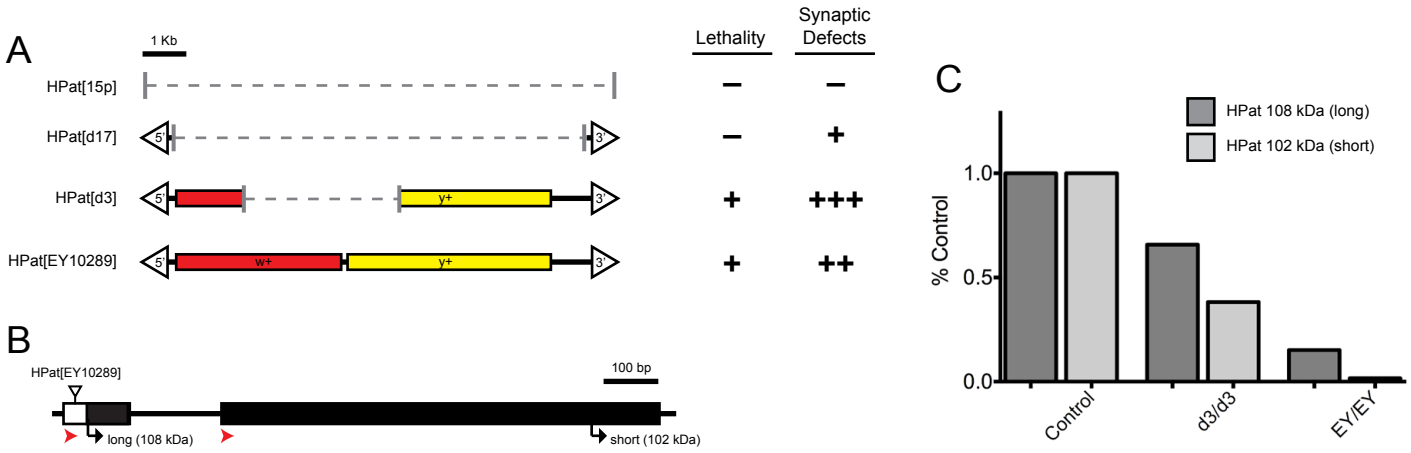

Fig. S1. *Drosophila* HPat alleles and isoforms. (A) Diagram of the *EY10289* insertion and the effect of each *hpat* allele on viability and synaptic morphology. In *hpatd3* a 3929 bp fragment spanning the central region of the P element was excised. In *hpatd17* a 10189 bp fragment was excised. In both cases, flanking P element sequence remains in the *hpat* 5'UTR. In contrast, *hpat15p* represents is a precise excision of the *EY10289* insertion. (B) Diagram of the 5' end of the *hpat* gene. Alternative transcriptional start sites (red arrowheads) can lead to the production of two isoforms of the HPat protein. (C) Relative expression levels of the 102 and 108 kDa isoforms of HPat in extract from whole *hpatd3* and *hpatEY10289* homozygous mutant larvae. HPat protein levels were normalized to a loading control (actin) and then to *w1118* controls.

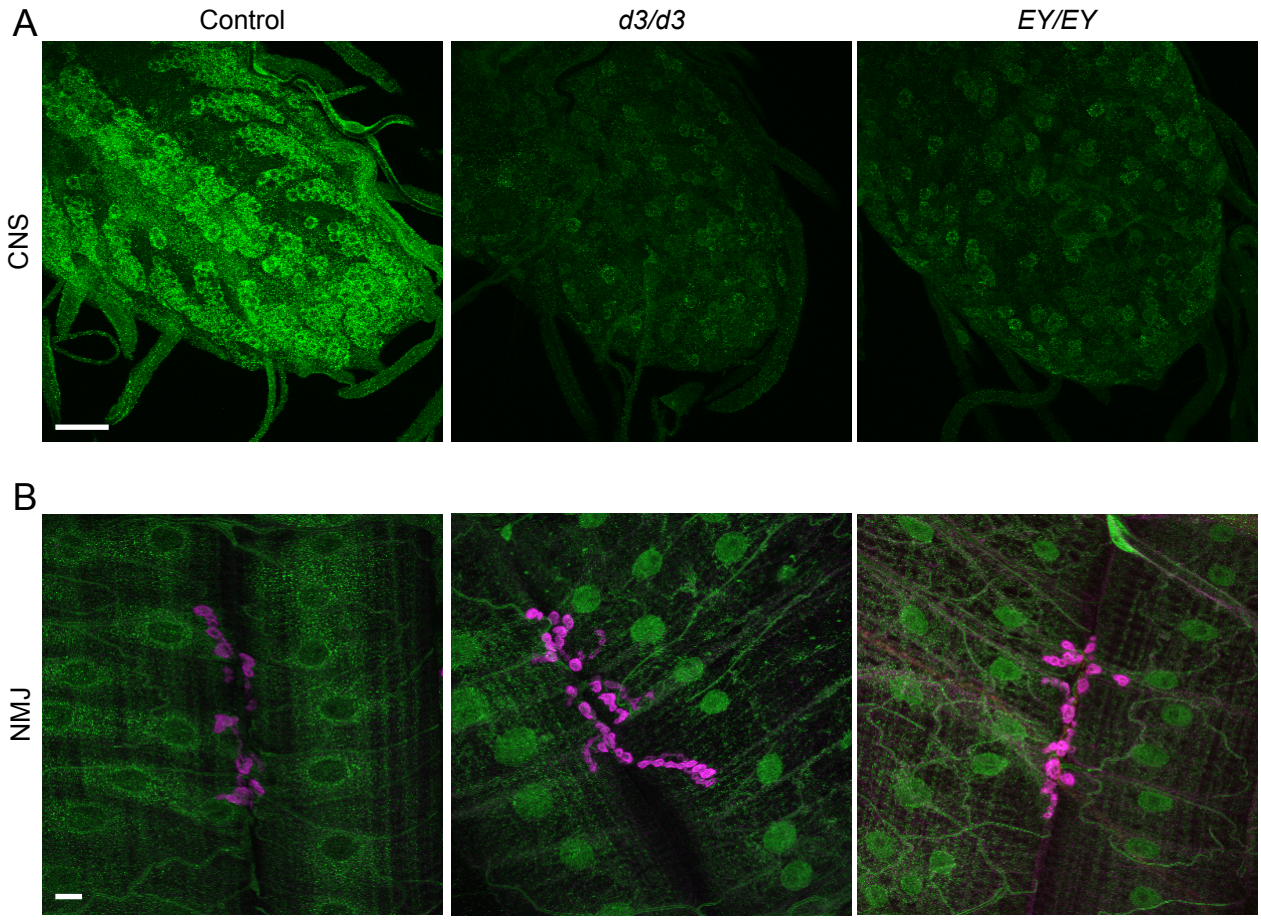

Fig. S2. Specificity of HPat antibodies. (A) *w1118* control, *hpatd3* and *hpatEY10289* homozygous13 mutant larval ventral ganglion and (B) NMJs stained with rat polyclonal antibodies against HPat (green) and postsynaptic Dlg (in NMJs only; magenta). Larvae from each genotype were dissected and processed together in the same dish. All images were collected using the same confocal settings. (A) Note three things in *hpat* mutant ventral ganglia. First, in contrast to western blots of larval extracts, overall HPat levels appear to be equally reduced in *hpatd3* and *hpatEY10289* mutants. Second, punctate cytoplasmic staining in the soma and neuropile of most neurons is significantly reduced. Finally, the pattern of HPat staining in the ventral ganglion is disrupted. Note that the control panel shows HPat staining in a single focal plane. In contrast, the *hpat* mutant panels are z-stacks through the entire ventral ganglion. Therefore, the intensity and pattern of HPat staining is likely to be overrepresented in *hpat* mutants compared to controls. (B) Punctate perinuclear staining in muscle is equally reduced in *hpat* mutants. There is also a distinct nuclear staining compared to controls. This is consistent with data suggesting that HPat orthologs can have a nuclear function (Marnef et al., 2011). All panels shown here are z-stacks through the entire NMJ. Very similar results in the CNS and at the NMJ were observed with rabbit polyclonal antibodies against HPat (data not shown). Scale bar = 20 µm.

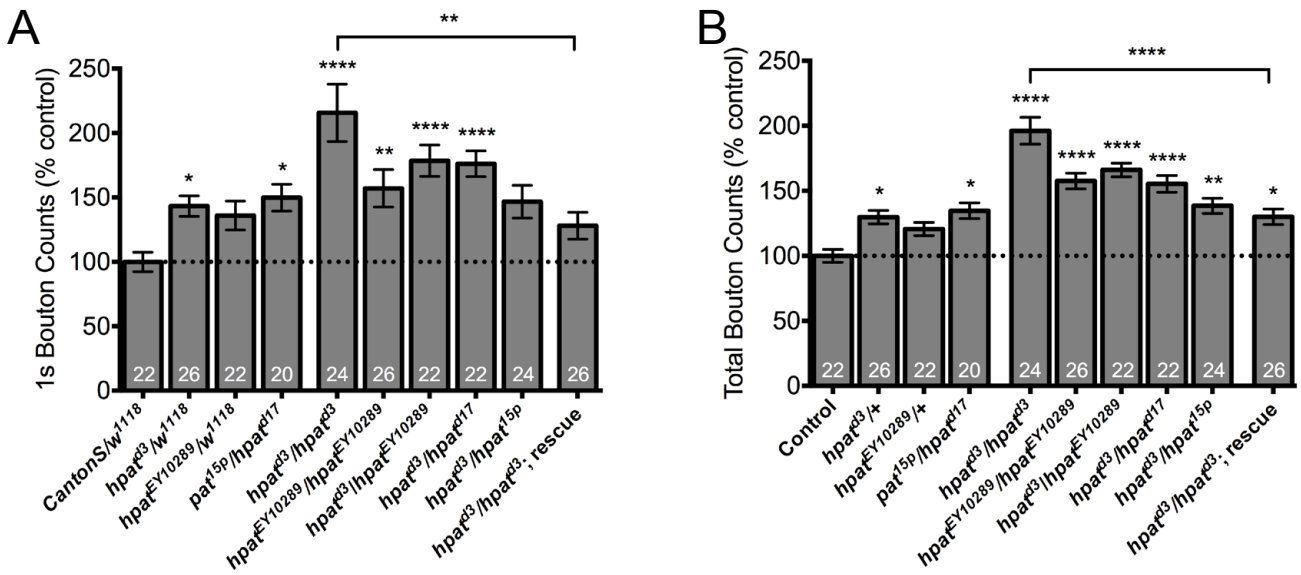

Fig. S3. HPat negatively regulates synaptic growth during larval development. Quantification of the number of (A) type 1s and (B) total synaptic boutons at muscle 6/7. Unless otherwise indicated, stars denote statistical significance compared 1 to *Canton-S/+* controls. (* $p < 0.05$; ** $p < 0.01$; *** $p < 0.001$; **** $p < 0.0001$; Kruskal-Wallis; Dunn's post-hoc test).

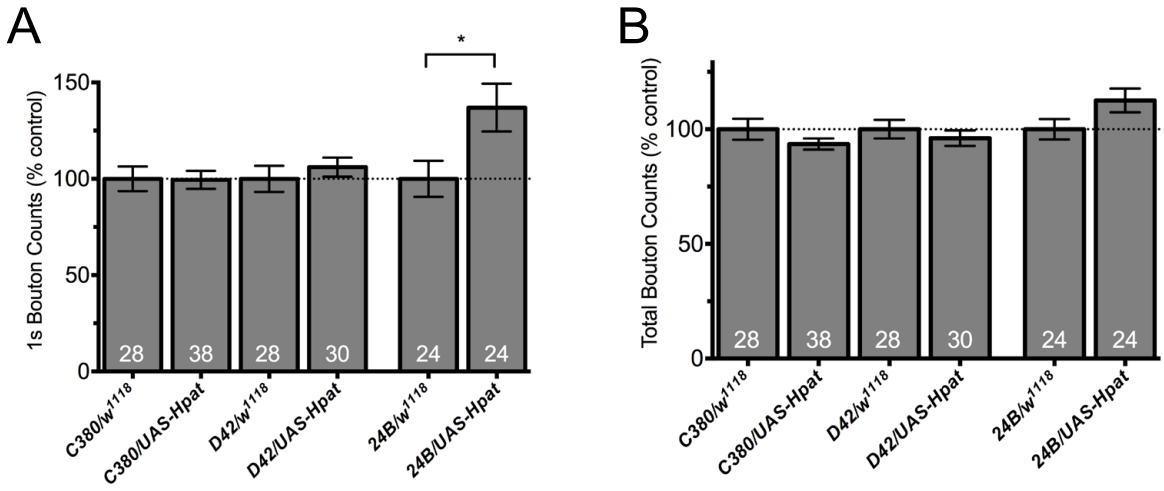

Fig. S4. HPat overexpression does not have a strong effect on synaptic growth during larval development. Quantification of the number of (A) type 1s and (B) total synaptic boutons at muscle 6/7 following pre- and postsynaptic overexpression of *hpat*. Stars indicate statistical significance compared to controls (* $p < 0.05$; Student's t-test).

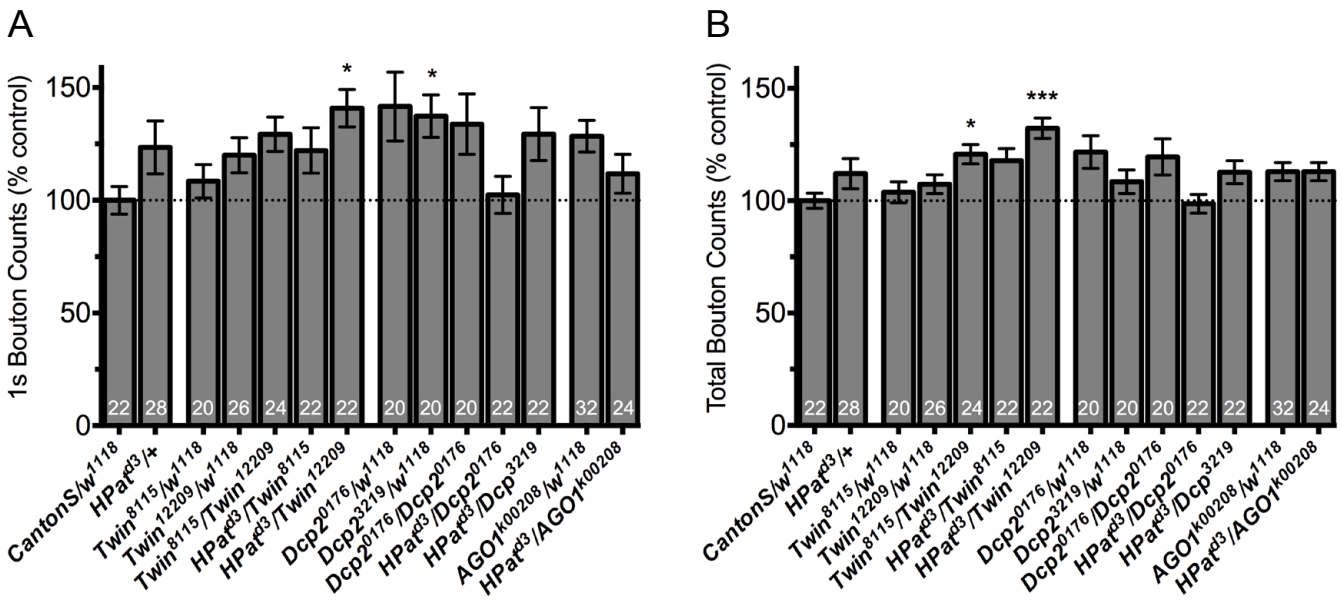

Fig. S5. HPat interacts with components of the deadenylase complex and miRNA pathway to control synaptic growth during larval development. Quantification of the number of (A) type 1s and (B) total boutons at muscle 6/7 clefts in genetic interaction experiments. Stars indicate statistical significance compared to the control (* $p < 0.05$; ** $p < 0.01$; *** $p < 0.001$; ****$p < 0.0001$; Kruskal Wallis; Dunn's post-hoc test).